

Dynamical stability analysis of the HD202206 system and constraints to the planetary orbits[★]

J. Couetdic¹, J. Laskar¹, A.C.M. Correia^{1,2}, M. Mayor³, and S. Udry³

¹ Astronomie et Systèmes Dynamiques, IMCCE-CNRS UMR 8028, Observatoire de Paris, UPMC, 77 avenue Denfert-Rochereau, 75014 Paris, France

² Departamento de Física, Universidade de Aveiro, Campus de Santiago, 3810-193 Aveiro, Portugal

³ Observatoire de Genève, 51 ch. des Maillettes, 1290 Sauverny, Switzerland

Preprint online version: June 15, 2018

ABSTRACT

Context. Long-term precise Doppler measurements with the CORALIE spectrograph revealed the presence of two massive companions to the solar-type star HD202206. Although the three-body fit of the system is unstable, it was shown that a 5:1 mean motion resonance exists close to the best fit, where the system is stable. It was also hinted that stable solutions with a wide range of mutual inclinations and low O-C were possible.

Aims. We present here an extensive dynamical study of the HD202206 system aiming at constraining the inclinations of the two known companions, from which we derive possible ranges of value for the companion masses.

Methods. We consider each inclination and one of the longitude of ascending node as free parameters. For any chosen triplet of these parameters, we compute a new fit. Then we study the long term stability in a small (in terms of O-C) neighborhood using Laskar's frequency map analysis. We also introduce a numerical method based on frequency analysis to determine the center of libration mode inside a mean motion resonance.

Results. We find that acceptable coplanar configurations (with low χ^2 stable orbits) are limited to inclinations to the line of sight between 30° and 90°. This limits the masses of both companions to roughly twice the minimum: $m_b \in [16.6 M_{Jup}; 33.5 M_{Jup}]$ and $m_c \in [2.2 M_{Jup}; 4.4 M_{Jup}]$. Non coplanar configurations are possible for a wide range of mutual inclinations from 0° to 90°, although $\Delta\Omega = 0[\pi]$ configurations seem to be favored. We also confirm the 5:1 mean motion resonance to be most likely. In the coplanar edge-on case, we provide a very good stable solution in the resonance, whose χ^2 does not differ significantly from the best fit. Using our method to determine the center of libration, we further refine this solution to obtain an orbit with a very low amplitude of libration, as we expect dissipative effects to have dampened the libration.

Key words. HD202206 - extra-solar planetary systems - mean motion resonance - frequency map analysis

1. Introduction

The CORALIE planet-search program in the southern hemisphere has found two companions around the HD202206 star. The first one is a very massive body with $17.5 M_{Jup}$ minimum mass (Udry et al. 2002), while the second companion is a $2.4 M_{Jup}$ minimum mass planet (Correia et al. 2005). The parent star has a mass of 1.044 solar masses, and is located 46.3 pc from the Solar System. The HD202206 planetary system is an interesting case to investigate the brown dwarf desert since the more massive companion can be either a huge planet (formed in the circumstellar disk) or a low-mass brown dwarf candidate.

Correia et al. (2005) found that the orbital parameters obtained with best fit for the two planets leads to a catastrophic events in a short time (two keplerians fit and full three-body fit alike). This was not completely unexpected given the very large eccentricities (0.435 and 0.267) and masses of the two planets. Using frequency analysis (Laskar 1990, 1993, 1999) they performed a study on the global dynamics around the best fit, and found that the strong gravitational interactions with the first

companion made the second planet evolution very chaotic, except for initial conditions in the 5:1 mean motion resonance. Since the associated resonant island actually lies close to the χ^2 minimum value of the best fit, they concluded that the system should be locked in this 5:1 resonance. Later on, Goździewski and co-workers also looked for stable solutions in this system using their GAMP algorithm (Goździewski et al. 2006). They provided two possible solutions (among many others), one coplanar, and one with a very high mutual inclination.

Since then, new data have been acquired using the CORALIE spectrograph. A new reduction of the data changed some parameters, including the mass of the HD202206 star. A new fit assuming a coplanar edge-on configuration was derived from the new set of radial velocity data. This new solution still appears to be in the 5:1 mean motion resonance, but is also still unstable. The most striking difference from Correia et al. (2005) is the smaller eccentricity of HD202206 c.

In the present work, we will continue in more detail the dynamical study started in Correia et al. (2005), using the new fit as a starting point. We also aim to find constraints on the orbital parameters of the two known bodies of this system, in particular the inclinations (and thus the real masses of the planets). Goździewski et al. (2006) already showed that stable fits could be obtained with different inclinations, using a particular fitting genetic algorithm that adds stability computation to select its

[★] Based on observations made with the CORALIE instrument on the EULER 1.2m telescope at La Silla Observatory under the ?? programme ID ?? . The table with the radial velocities is available in electronic form at the CDS via anonymous ftp to cdsarc.u-strasbg.fr (130.79.128.5) or via <http://cdsweb.u-strasbg.fr/cgi-bin/qcat?J/A+A/???>

populations (GAMP). Although very effective in finding a stable fit, this algorithm cannot find all possible solutions. We prefer here an approach which separates the fitting procedure from dynamical considerations, as it allows for a better assessment of the goodness of the fit, and whether the model is a good description of the available data. The trade-off is a more difficult handling of the high number of parameters.

We briefly present the new set of data in Sect. 2, the numerical methodology in Sect. 3. We review in details the dynamics in the coplanar edge-on case in Sect. 4. We then release the constraint on the inclination of the system from the line of sight in Sect. 5, and finally briefly investigate the mutually inclined configurations in Sect. 6.

2. New orbital solution for the HD202206 system

Table 1. Best Newtonian fit **S1** for the HD202206 system assuming $i_b = i_c = 90^\circ$, and $\Delta\Omega = 0^\circ$.

Param.	S1	inner	outer
V_0	[km/s]	14.729 ± 0.001	
P	[days]	256.389 ± 0.044	1397.445 ± 19.056
K	[m/s]	564.82 ± 1.42	38.08 ± 1.21
e		0.431 ± 0.001	0.104 ± 0.024
ω	[deg]	161.91 ± 0.27	105.56 ± 15.77
$M + \omega$	[deg]	239.016 ± 0.13	250.38 ± 2.71
a	[AU]	0.8053	2.4832
i	[deg]	90	90
Ω	[deg]	0	0
m	[M_{Jup}]	16.59	2.179
Date	[JD-2400000]	53000.00	
rms	[m/s]	7.4544	
$\sqrt{\chi_r^2}$		1.411	

Errors are given by the standard deviation σ . This fit corresponds to a coplanar system seen edge-on, with minimum values for the masses.

The CORALIE observations of HD202206 started in August 1999 and the last point acquired in our sample dates from September 2006, corresponding to about seven years of observations and 92 radial-velocity measurements. Using the iterative Levenberg-Marquardt method (Press et al. 1992), we fit the observational data using a 3-body Newtonian model, assuming co-planar motion perpendicular to the plane of the sky, similarly to what has been done in (Correia et al. 2005; Correia et al. 2009b). Notice that we changed the reference date with respect to the solution in Correia et al. (2005). The mass of the star has also been updated to $1.044 M_\odot$ (Sousa et al. 2008). This fit yields two planets with an adjustment of $\sqrt{\chi_r^2} = 1.41$ and $rms = 7.45 \text{ ms}^{-1}$, slightly above the photon noise of the instrument which is around 6.69 ms^{-1} . We confirm the already detected planets (Udry et al. 2002; Correia et al. 2005) with improved orbital parameters, one at $P = 254.8$ day, $e = 0.431$, and a minimum mass of $16.6 M_{\text{Jup}}$, and the other at $P = 1397$ day, $e = 0.104$, and a minimum mass of $2.18 M_{\text{Jup}}$ (Table 1). In figure 1 we plot the observational data superimposed on the best fitted solution.

We also fitted the data with a 3-body Newtonian model for which the inclination of the orbital planes, as well as the node of the outer planet orbit, were free to vary. We were able to find a wide variety of configurations, some with low inclination values for one or both planets, that slightly improved our fit to a minimum $\sqrt{\chi_r^2} = 1.30$ and $rms = 7.08 \text{ m/s}$. However, all of these

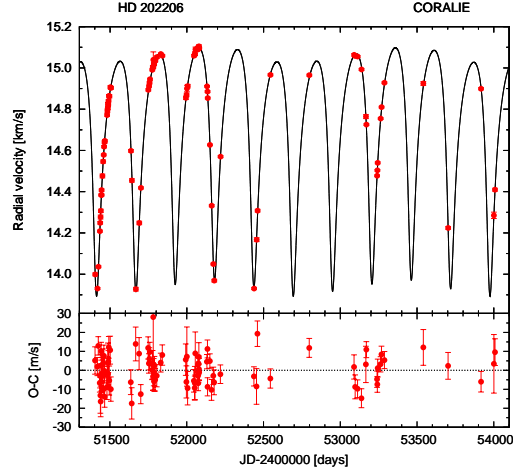


Fig. 1. CORALIE radial velocities for HD 202206 superimposed on a 3-body Newtonian orbital solution (Table 1).

determinations remain uncertain, and since we also increase the number of free parameters by three, we cannot say that there has been an improvement with respect to the solution presented in Table 1.

3. Numerical set-up

3.1. Conventions

In this paper, the subscripts b and c will respectively refer to the body with shortest and longest orbital period (inner and outer). The initial conditions ill-constrained by the radial velocity data are $i_b, i_c, \Omega_b, \Omega_c$ (the inclinations, and longitude of ascending nodes). We are using the observers convention which sets the plane of sky as the reference plane (see fig 2). As a consequence, the nodal line is in the plane of sky, and has no cinematic impact on the radial velocities. From the dynamical point of view, only the difference between the two lines of nodes $\Delta\Omega$ matters. In particular the mutual inclination depends on this quantity, through:

$$\cos I = \cos i_b \cos i_c + \sin i_b \sin i_c \cos \Delta\Omega. \quad (1)$$

Ω_b can thus always be set to 0° in the initial conditions, which leads to $\Delta\Omega = \Omega_c$, and only three parameters are left free (i_b, i_c, Ω_c). They are connected to the three interesting unknowns of the system, namely the mutual inclination I (Eq. 1), and the two planetary masses m_b, m_c as:

$$\begin{cases} \frac{m_b(m_* + m_b)^{1/3}}{m_* + m_b + m_c} = \frac{K_b P_b^{1/3} \sqrt{1 - e_b^2}}{(2\pi G)^{1/3} \sin i_b}, \\ \frac{m_c(m_* + m_c)^{1/3}}{m_* + m_b + m_c} = \frac{K_c P_c^{1/3} \sqrt{1 - e_c^2}}{(2\pi G)^{1/3} \sin i_c}, \end{cases} \quad (2)$$

where m_* is the star mass, K_σ the amplitude of the radial velocity variations, P_σ the orbital period, e_σ the eccentricity, and G the gravitational constant. Basically, choosing the values of the inclinations is akin to setting the two companions masses. And for given values of (i_b, i_c), we can control the mutual inclination with Ω_c through Eq. 1.

Note that the denominator on the left hand sides in Eq. 2 is the total mass of the system. This term comes from the transformation to the barycentric coordinates system. As a consequence, the two equations are coupled. Of course, we can usually neglect

where $\mu = Gm_*/c^2$, n is the mean motion, and $\eta = \sqrt{1 - e^2}$. These equations are averaged to obtain the following first order secular perturbations:

$$\begin{aligned} \langle \dot{a} \rangle &= 0, \\ \langle \dot{e} \rangle &= 0, \\ \langle \dot{M} \rangle &= \frac{\mu n}{a} \left[6 - \frac{15}{\sqrt{1 - e^2}} \right], \\ \langle \dot{\omega} \rangle &= \frac{3\mu n}{a(1 - e^2)}. \end{aligned} \quad (6)$$

These corrections are computed every 100 steps, that is every two years, with the current values at the given step for e , a and n , for each planet. These approximated equations have been successfully tested by comparison with INPOP (Fienga et al. 2008).

3.4. Stability threshold

In order to study the stability of a given orbit, we use Laskar's frequency map analysis (Laskar 1990, 1993). Using a numerical integration of the orbit over a time interval of length T , we compute a refined determination (in $^\circ/\text{yr}$) of the mean motions n_1 , n'_1 obtained over two consecutive time intervals of length $T_1 = T/2$. The stability index $D_1 = |n'_1 - n_1|$ provides a measure of the chaotic diffusion of the trajectory. Small values close to zero correspond to a regular solution while high values are synonymous of strong chaotic motion (Laskar 1993).

In this paper we look at many different orbits for many different initial conditions to detect stable regions. This calls for a way to automatically calibrate a threshold for stability D_{lim} . To that end we use a second stability index D_2 . Using the same numerical integration, we compute two new determinations of the mean motion n_2 and n'_2 over two consecutive time intervals of length $T_2 = T_1/k$, where $k > 1$. In the case of quasi-periodic motion, the diffusion should be close to zero but it is limited by the precision of the determination of the frequencies. Since D_1 is computed over longer time intervals, the frequencies are better determined, and thus, D_1 should be, on average, smaller than D_2 . On the contrary, for chaotic trajectories, the diffusion will increase on average for longer time intervals. We can then determine an approximated value D_{lim} for which:

$$\begin{cases} D_1 \gg D_{\text{lim}} \implies D_1 > D_2, \\ D_1 \ll D_{\text{lim}} \implies D_1 < D_2. \end{cases} \quad (7)$$

We will then be assured that the first kind of orbits is in general stable, while the latter is considered chaotic.

This approach is best used statistically over a grid of initial conditions, especially when we try to use a small integration time. In order to determine D_{lim} for a particular diffusion grid, we look at the distribution of $D_1 < D_2$ trajectories as a function of D_1 . We actually work with smoothed values D_1^s and D_2^s of D_1 and D_2 to reduce the influence of the chaotic orbits whose mean motion diffusions are small by mere chance. They appear as low diffusion orbits inside high diffusion region. The smoothing function is a simple geometric mean over the closest neighbors. Other functions, such as a convolution with 2D Gaussian, have been tested, but do not yield significantly better results.

We bin the $\log D_1^s$ data in 0.5 wide bins, and compute for each bin the percentage of $D_1^s < D_2^s$ orbits. Fig. 3 shows a typical distribution obtained from a diffusion grid (in this case the top panel of figure 6). It reproduces the behavior expected from

Eq. 7: low diffusion orbits tend, in great majority, to have their diffusion index diminish when time increases.

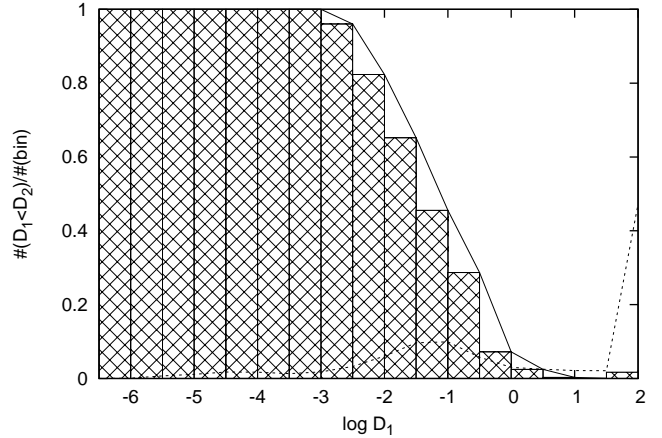


Fig. 3. Distribution of $D_1 < D_2$ trajectories from the top panel of Fig. 6. Each trajectory integrated is binned with respect to its diffusion index $\log D_1$, after the diffusion grid has been smoothed. For each bin we compute the proportion of trajectories with a decreasing diffusion index over time: $D_1 < D_2$. The histogram shows the results for 0.5 wide bins. As expected from equation 7, orbits with a high diffusion index D_1 , and $D_1 < D_2$ are nearly inexistent ($\log D_1 > -1$), while we observe the opposite situation for low diffusion index orbits ($\log D_1 < -3$).

We choose to define D_{lim} as the D_1 value for which 99% of the trajectories exhibit $D_1 < D_2$. Graphically, it is the abscissa for which the curve in Fig. 3 crosses $y = 0.99$. In this example we get $\log D_{\text{lim}} \approx -2.87$.

The 99% threshold is actually a compromise that works in the majority of encountered cases: it minimizes the number of orbits wrongly flagged as stable (false stable) or unstable (false unstable). This is also approximately the value for which the number of false stables and false unstables is equivalent. For percentages lower than 95% the number of false unstables is nearly null. It is easy to understand since a higher percentage threshold implies a lower value for D_{lim} , which in turns leads to very few actually unstable orbits flagged, while we might miss several stable ones, and vice-versa. To estimate the number of false stables and unstables, we recomputed the diffusion grid on a longer integration time, 2×40000 years, and use this grid as a reference (Fig. 4).

4. Review of the coplanar edge-on case

4.1. Global dynamics

Following Correia et al. (2005), we will study in more details the dynamics in the neighborhood of the 3-body fit obtained in the case of coplanar orbits with $\sin i_b = \sin i_c = 1$ (that is, the system seen edge-on). The best fit to the radial velocity data for this particular configuration is given in table 1. It is different from the solution **S4** in Correia et al. (2005) (Table 4) as explained in Sect. 2. For the dynamical aspect of the system, the important change is the decrease in planet c's eccentricity. As a consequence regions outside resonances are expected to be more stable, and the environment of the fit should be less chaotic. However this new solution is still unstable: the outer planet is lost shortly after about 150 millions years.

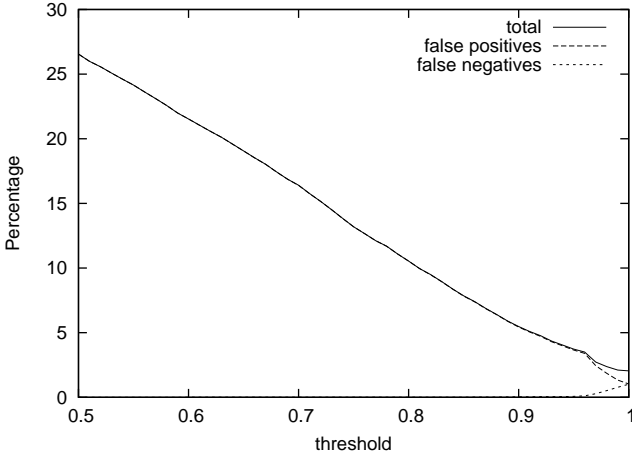


Fig. 4. Percentage of orbits wrongly flagged stable (false stable) or unstable (false unstable). Once D_{lim} is chosen using a given percentage threshold (see figure 3), we have a criterion for stable ($D_1 < D_{\text{lim}}$) and unstable orbits ($D_1 > D_{\text{lim}}$). We compare the results with a diffusion grid computed over a longer time interval (in this case 2×40000 years) taken as a reference. A few orbits deemed stable from the reference diffusion grid were thought to be unstable and vice versa. The solid line traces the number of those faulty orbits for different values of the threshold. It appears to be minimum between 0.95 and 1. The dotted line traces the false positives, and the dashed line, the false negatives (the solid one is the sum of those two).

We look for possible nearby stable zones, keeping HD202206b parameters constant since they are much better constrained, with small standard errors. We assume for now that the system is coplanar and seen edge-on, that is with both inclination at 90° , and $\Omega_c = 0^\circ$. We let a_c , e_c , and ω_c vary. We always keep $M_c + \omega_c$ constant as it is much better constrained by the radial velocity data. This implies that when we change ω_c , the mean anomaly M_c varies accordingly. In the particular case where $\Omega_c = 0^\circ$, this means that the initial mean longitude λ_c is kept constant. For each initial conditions we compute the diffusion index $\log D_1$, and the square root of the reduced χ^2 .

Fig. 5 shows a global picture of the dynamics around the fit, in the planes (a_c, e_c) and (a_c, ω_c) of initial conditions. The step-sizes for a_c , ω_c , e_c are respectively 0.005 AU , 2° and 0.004 . The other parameters were kept constant and taken from the fit **S1** (Table 1). The level curves give the $\sqrt{\chi_r^2}$ value computed for each set of initial conditions. The color scale gives the diffusion index $\log D_1$. The yellow to red areas are very chaotic, mainly due to the large eccentricities and masses of both planets.

The orbital solution **S1** lies inside the $\sqrt{\chi_r^2} = 1.5$ level curves, at the coordinates marked by a cross, inside a high diffusion (green) area. Several low diffusion (blue and dark blue) zones exist for which the orbits are stabilized either by mean motion resonances, or by locking of $\Delta\varpi$ around 0° . Orbits stabilized by the corotation of the apsidal lines are the blue to black zones around $\omega_c = 190^\circ$ (bottom panel). The width (in the ω_c direction) increases with the semi-major axis a_c , from 90 degrees at 2 AU, to nearly 360 degrees at 4 AU, since a wider libration of $\Delta\varpi$ around 0° is possible without close encounters when the distance between the two planets increases. The red to green more or less vertical stripes cutting through these zones mark mean motion resonances, which for the most part have a destabiliz-

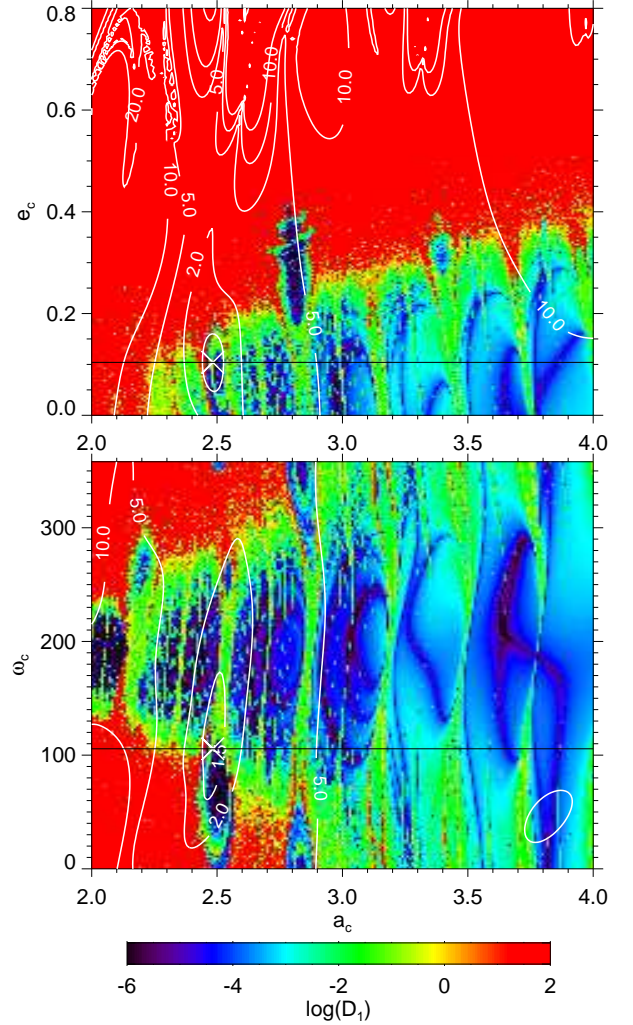


Fig. 5. Global view of the dynamics of HD202206 for variation of the semi-major axis and periastrum of the outer planet (bottom panel) or semi-major axis and eccentricity (top panel). The step-sizes for a_c , ω_c , e_c are respectively 0.005 AU , 2° and 0.004 . The other parameters were kept constant and taken from the fit **S1** (Table 1). The color scale is the stability index $\log D_1$ obtained through a frequency analysis of the longitude of the outer planet over two consecutive time intervals of 8000 years. The level curves give the $\sqrt{\chi_r^2}$ value computed for each choice of parameters. The two horizontal black lines mark the intersection of the two grids. Most of the orbits are chaotic (yellow to red dots), but regular orbits zones exist (blue dots). One of these regular orbits regions lies inside the low $\sqrt{\chi_r^2}$ region: the dark area around $a_c = 2.5 \text{ AU}$ and $\omega_c = 50^\circ$. It corresponds to the stable island of the $1/5$ mean motion resonance. The cross marks the **S1** orbital solution.

ing effect in the two plans considered in Fig. 5. However, the stronger ones also have stable orbits:

- the $1/4$ MMR at 2.2 AU with two stable islands around $\omega_c = 260^\circ$ and $\omega_c = 50^\circ$.
- the $5:1$ MMR at 2.5 AU with a notable stable island around $\omega_c = 70^\circ$ where the best fit is located.
- the $1/6$ MMR at 2.8 AU with a stable island around $\omega_c = 0^\circ$ or high eccentricity.

4.2. Stable fit

We now take a closer look at the 5:1 mean motion resonance island around $a_c = 2.5$ AU and $\omega_c = 50^\circ$, where we believe the system is presently locked. Fig. 6 was constructed the same way as Fig. 5, but the step-sizes are now 0.0025 AU for a_c , 0.5° for ω_c , and 0.002 for e_c .

For eccentricities higher than 0.2, orbits are very chaotic (red dots), as the outer planet undergoes close encounters with the inner body. At lower eccentricities we notice some lower diffusion orbits for $\omega_c > 120^\circ$. Those orbits lie far outside the resonance, but may be stable because of the low eccentricity of the outer planet, and apsidal locking mechanism. They are however too far from the best fit ($\sqrt{\chi_r^2} > 1.5$) and are less likely to be a good guess of the actual configuration of HD202206 system.

A very noticeable feature of this resonant island appearing in both panel, is the existence of two distinct stable regions, separated by chaotic orbits inside the resonance itself. The two stable regions actually correspond to two different critical arguments: $\lambda_b - 5\lambda_c + 4\varpi_c$ in the structure on the rim, and $\lambda_b - 5\lambda_c + \varpi_b + 3\varpi_c$ in the center.

The orbital solution **S1** (white cross) lies very close to the latter, in a chaotic region (green and yellow dots) between the two stable parts of the resonant island. In fact, one can pick stable orbits with a $\sqrt{\chi_r^2}$ not significantly worse than the best fit. For instance, the orbital solution **S2** given in table 2 is stable and has a $\sqrt{\chi_r^2}$ of 1.4136 (marked by a filled white circle). The orbital elements are the same as **S1**, except for a_c which was adjusted from 2.4832 AU to 2.49 AU.

Table 2. Stable orbital parameters **S2** for the HD202206 system for $i_b = i_c = 90^\circ$ and $\Delta\Omega = 0^\circ$. Using the fit **S1** as a starting point (Table 1), we select a value for the semi-major axis of the outer planet such that the system becomes stabilized in the 5:1 mean motion resonance. This orbit is marked by a white filled circle in Fig. 6.

Param.	S2	inner	outer
a	[AU]	0.8053	2.49
i	[deg]	90	90
e		0.431	0.104
$M + \omega$	[deg]	239.016	250.38
ω	[deg]	161.91	105.56
Ω	[deg]	0	0
m	[M_{Jup}]	16.59	2.179
Date	[JD-2400000]	53000.00	
$\sqrt{\chi_r^2}$		1.4136	

4.3. Resonant and secular dynamics

The orbital solution **S2** was integrated over 5 Gyr. It remained stable, and displays a regular behavior during the whole time.

Using frequency analysis on an integration over 1Myr, we determined its fundamental frequencies (table 3). Following our notation, n_b and n_c are the mean motions. The secular frequencies are noted g_1 and g_2 . Finally l_θ is the frequency associated with the resonance’s critical angle θ . The fundamental secular frequencies g_1 and g_2 , related to the periastron of the inner and outer planet, correspond to the periods $P_1 \approx 14.1 \times 10^3$ yr and $P_2 \approx -791$ yr (the periastron of the outer planet is retrograde).

Due to the mean motion resonance, a linear relation links the first four fundamental frequencies in Table 3: $n_b - 5n_c + g_1 +$

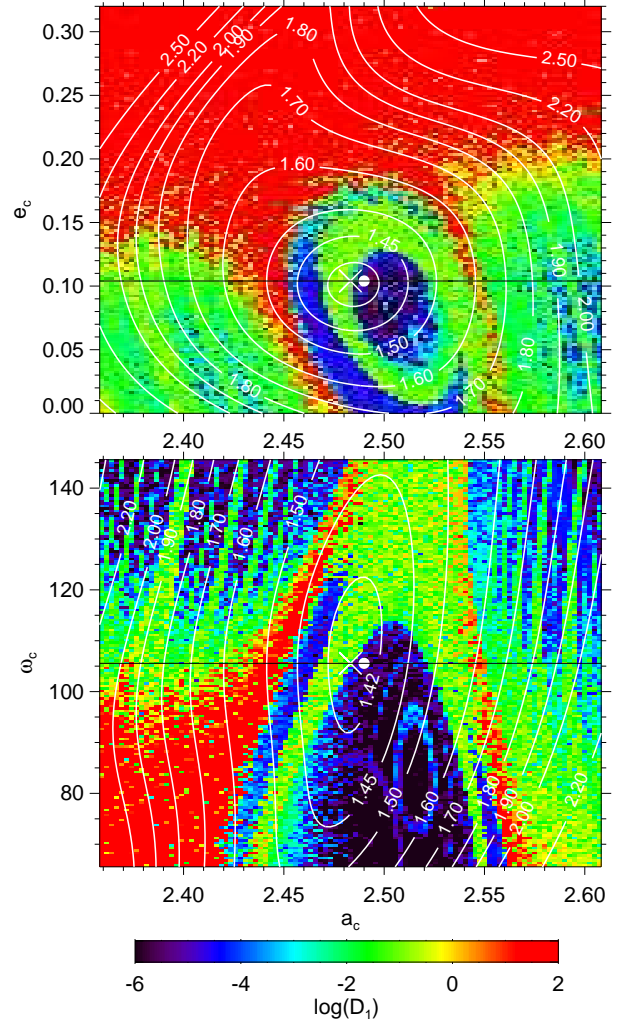


Fig. 6. Global view of the dynamics of HD202206 for variation of the semi-major axis and periastron (bottom), and semi-major axis and eccentricity (top) of the outer planet. The step-sizes are respectively 0.0025 AU, 0.5° , and 0.002 for the eccentricity. The color scale is the stability index ($\log D_1$), and the level curves give the $\sqrt{\chi_r^2}$ values (see Fig. 5). The cross marks the best fit **S1**, and the horizontal line in each panel, the orbits common to both maps (ie. the intersection of each map). The best fit lies very close to a stable resonant island where we can pick a stable solution with a χ^2 only marginally higher than that of the best fit. As an example we picked such a solution (**S2**), marked by a white filled circle, by slightly increasing a_c from 2.4832 AU to 2.49 AU. The complete set of orbital elements for **S2** is given in Tab.2

$3g_2 = 0$. As a consequence, one of them is superfluous. A new fundamental frequency associated to the resonance l_θ replaces it.

The solution **S2** is trapped in the 5:1 mean motion resonance with the following main resonant argument:

$$\theta = \lambda_b - 5\lambda_c + \varpi_b + 3\varpi_c . \tag{8}$$

The variations of θ versus time are plotted in Fig. 7 (green line) and exhibit a libration around $\theta_0 = 0^\circ$. We observe nonetheless that this libration is the modulation of several different terms with similar amplitudes of approximately 40° , but on different time scales. This leads to a libration with an amplitude that can be higher than 180° .

Table 3. Fundamental frequencies for **S2**. n_b and n_c are the mean motions, g_1 and g_2 are the secular frequencies associated with respectively ϖ_b and ϖ_c , and l_θ is the libration frequency of the resonant angle $\theta = \lambda_b - 5\lambda_c + \varpi_b + 3\varpi_c$.

	Frequency °/yr	Period yr
n_b	513.157691	0.70
n_c	102.363620	3.52
g_1	0.025537	14097.19
g_2	-0.455042	791.13
l_θ	4.492737	80.13

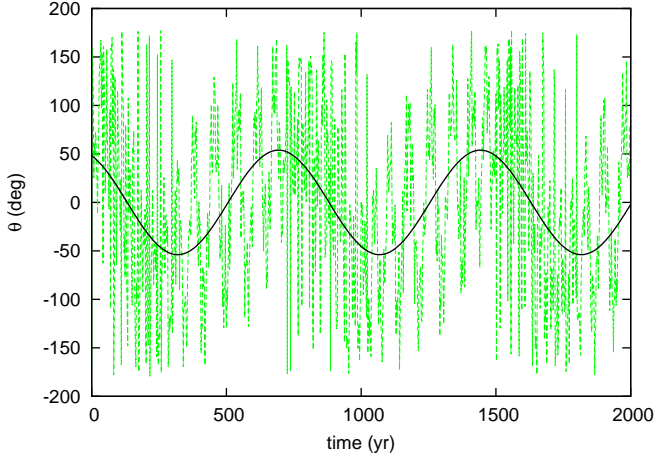


Fig. 7. Time variation of the resonant argument $\theta = \lambda_b - 5\lambda_c + \varpi_b + 3\varpi_c$ for the orbital solution **S2** (green line). θ is in libration around $\theta_0 = 0^\circ$, with a modulation of two terms of period $P_\theta = 80.13$ years, and $P_{\Delta\varpi} = 749.10$ years, amplitudes of about 35 and 50 degrees respectively. The black line shows the first secular term contribution.

In order to describe more accurately the behavior of θ , we search for a quasi-periodic decomposition of $\theta(t)$. We start with a frequency decomposition using frequency analysis (Laskar 2003) as:

$$\theta(t) = \sum_j A_j \cos(\nu_j t + \phi_j) \quad (9)$$

And then we decompose each frequency ν_j on the four fundamental frequencies (n_c, g_1, g_2, l_θ):

$$\nu_j = \alpha_j n_c + \beta_j g_1 + \delta_j g_2 + \gamma_j l_\theta, \quad (10)$$

where $\alpha_j, \beta_j, \delta_j$, and γ_j are integers. Each term of the decomposition follows a D'Alembert-like relationship expressed in Eq. 11.

$$\alpha_j + \beta_j + \delta_j = 0 \quad (11)$$

which can be used to simplify the expression of ν_j . Indeed rearranging the right hand side of Eq. 10, we can write:

$$\nu_j = \alpha_j n_c + \beta_j (g_1 - g_2) + (\beta_j + \delta_j) g_2 + \gamma_j l_\theta, \quad (12)$$

and using Eq. 11, we get:

$$\nu_j = \alpha_j (n_c - g_2) + \beta_j (g_1 - g_2) + \gamma_j l_\theta. \quad (13)$$

The first thirty terms of the decomposition can be found in Table 4. The decrease of the amplitudes A_j is slow, due to the strong perturbations.

Table 4. Quasi-periodic decomposition of the resonant angle $\theta = \lambda_b - 5\lambda_c + \varpi_b + 3\varpi_c$ for an integration of the orbital solution **S2** over 1 million years. The decomposition is given in the form given by Eq. 9, and each frequency ν_j is expressed as a combination of the fundamental frequencies in the form given by Eq. 13. For the sake of brevity, we only give the first 30 terms.

j	ν_j , deg/yr	A_j , deg	ϕ_j , deg	α_j	β_j	γ_j
1	0.480579	53.892	26.688	0	1	0
2	4.973316	36.043	-132.474	0	1	1
3	4.492737	34.786	111.145	0	0	1
4	4.012157	21.409	-5.446	0	-1	1
5	0.961158	21.399	-36.372	0	2	0
6	-512.651573	17.254	127.883	-5	3	0
7	-513.612733	16.069	-104.463	-5	1	0
8	5.934475	16.268	-79.250	0	3	1
9	6.415054	16.795	37.274	0	4	1
10	-522.430683	15.118	85.394	-5	-8	-1
11	-512.170994	12.658	64.316	-5	4	0
12	5.453895	12.716	-16.043	0	2	1
13	-513.132153	12.432	11.782	-5	2	0
14	-503.833622	11.911	117.837	-5	12	1
15	8.817951	11.908	79.987	0	9	1
16	205.156746	12.090	25.645	2	-1	0
17	-521.950104	10.953	21.911	-5	-7	-1
18	-522.911263	10.799	149.019	-5	-9	-1
19	-505.755940	11.882	-168.212	-5	8	1
20	-504.314203	9.299	-178.391	-5	11	1
21	-503.353041	8.914	53.782	-5	13	1
22	-505.275360	10.486	127.883	-5	9	1
23	102.818662	10.628	116.261	1	0	0
24	1018.888092	9.462	-112.965	10	-10	-1
25	6.895632	10.657	-25.001	0	5	1
26	307.975409	8.924	-128.711	3	-1	0
27	3.531578	8.135	-122.054	0	-2	1
28	7.376215	8.880	88.862	0	6	1
29	1025.783728	7.756	-49.947	10	-5	0
30	-411.274650	7.376	165.597	-4	0	0

The first term ($j = 1$) is responsible for the long term oscillations with frequency $g_1 - g_2$. The period corresponding to the angle $\Delta\varpi = \varpi_b - \varpi_c$, is $P_{\Delta\varpi} \approx 749.09$ years. It is worth mentioning that the angle $\Delta\varpi$ is not in libration in this system, as opposed to what has been observed in planetary systems locked in a $1/2$ mean motion resonance, such as GJ876 (Laughlin & Chambers 2001; Lee & Peale 2002; Ji et al. 2002; Correia et al. 2009a) or HD89830 (Goździewski & Maciejewski 2001), or in a $3/2$ mean motion resonance such as HD45364 (Correia et al. 2009b). The second one ($j = 2$) introduces the short term oscillations of frequency l_θ , corresponding to a period $P_\theta \approx 101.49$ years. More precisely the libration of θ is made of three different kinds of contributions:

- secular terms: $\alpha_j = \gamma_j = 0$, hence of the form $\beta_j (g_1 - g_2)$;
- resonant terms: $\alpha_j = 0$ and $\gamma_j \neq 0$, of the form $\beta_j (g_1 - g_2) + \gamma_j g_\theta$;
- and short period terms: $\alpha_j \neq 0$.

We plotted with a solid line in Fig. 7 the contribution of the term $j = 2$, the first secular contribution.

4.4. Test particles

We test in this section the possibilities for a third body around HD202206. To that end we integrate the **S2** solution with added massless particles over 16000 years. As explained in the previous sections, we compute two determinations n and n' of each

particles mean motion over two consecutive time intervals of 8000 years. We then obtain a stability index $D = \log |n - n'|$ for each particle, which we plotted with a color code in Fig. 8. Both panels are (a, e) grids of initial conditions of the test particles. We vary the semi-major axis from 0.05 AU to 0.5 AU with a 0.0025 step size in the left panel, and from 0.5 AU to 10 AU with a 0.05 step size in the right panel. We span eccentricities of the test particles from 0 to 0.9 with a 0.005 step size. Since the particles mean motions are higher in the left panel, they were integrated with a time step of 10^{-3} years instead of 2×10^{-3} .

Due to the very large eccentricities of HD202206 b and HD202206 c, the dynamical environment between and around them is very unstable. As a result, we don't expect any viable planets with a semi-major axis between approximately 0.12 AU and 6.5 AU (red dots). Most of these particles were actually lost before the end of the integration, either through collision or by having their eccentricity increased higher than 1. The same computation with particles of one Earth mass yields very similar results. Assuming that **S2** is a good representation of the HD202206 planetary system, we can use these results to put constraints on hypothetical and yet undetected additional companions. There is clearly two possible regions for new planets: either close to the star ($a < 0.12$ AU), or outside HD202206 c ($a > 6.5$ AU).

In the first case, any planet massive enough should already have been detected as many full period are available in the data. Assuming a low eccentricity for the hypothetical companion and a 6 m/s instrumental precision we find that planets bigger than 24 earth masses should have already been detected. A Neptune-sized planet can exist anywhere between 0.06 AU and 0.12 AU, and a 10 earth masses planet, anywhere between 0.02 AU and 0.12 AU.

In the second case ($a > 6.5$ AU) the period is greater than 16 years, meaning that we have only covered approximately half an orbit at best. However a planet massive enough would create at least a detectable trend in the data. At 6.5 AU we can rule out the existence of a planet with more than half a Jupiter mass. At 10 AU we can rule out a planet between $1 M_{Jup}$ and $3 M_{Jup}$, depending on the phase. We conclude that a yet undetected planet smaller than half a Jupiter mass could exist at semi-major axis greater than 6.5 AU.

4.5. Finding the center of libration inside a resonance through frequency analysis

4.5.1. Center of libration

We will consider in this section the planar three-body problem, and more particularly, the planetary problem with a $p : p + 1$ mean-motion resonance. The problem is to find the orbit center of libration starting from a quasi-periodic orbit in the resonance.

In the restricted case this center of libration is a well defined periodic orbit, such as the Lagrangian points in the 1 : 1 resonance. However in the general problem it is not so easy to define and to find this orbit. It has 4 degrees of freedom, and its quasi-periodic orbits live on 4-torus in the phase space. It should be noted that the problem can be restricted to 3 degrees of freedom, using the angular momentum reduction. Each dimension of the 4-torus is associated to one of the four fundamental frequencies (f_0, f_1, f_2, f_3) of the orbit. Let's suppose that f_0 is the frequency of the resonant mode. The orbit equivalent to the center of libration is living on a 3-torus, depending only on (f_1, f_2, f_3) . In other words, it is a torus where the fourth dimension associated to the resonance has a null amplitude. Intuitively, we can represent it

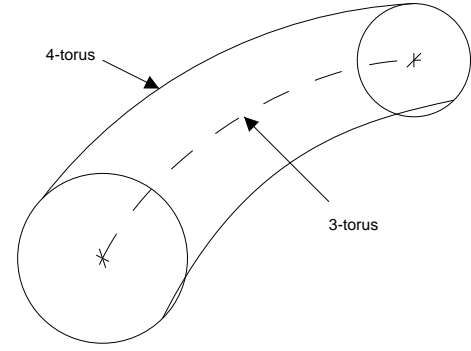


Fig. 9. Schematic representation of the 3-torus of the center of libration. We represent the 4-torus of a given resonant orbit by a 2-torus (a doughnut) as it is not possible to represent it otherwise. The center of libration 3-torus is then represented by the circle in the center of the interior of the doughnut.

has the center of the 4-torus in the dimension associated with the resonance.

4.5.2. Quasi-periodic decomposition

If this orbit was periodic we could use a simple Newton algorithm to find it (provided that we start within the convergence radius), as it is a fixed point of a Poincaré map. This method has been extensively used in numerical search of periodic orbit families of the three body problem (see for instance Henon 1974, 1997).

We present here a new numerical method to find quasi-periodic center of libration, using the fact that we can get an accurate quasi-periodic decomposition of a numerically integrated quasi-periodic orbit with frequency map analysis (Laskar 2003). Let $\mathbf{X}(t)$ be a state vector of such an orbit. Using frequency analysis, we can obtain a quasi-periodic representation for any component x of the vector \mathbf{X} :

$$x(t) = \sum_{(k)} A_{(k)} E^{i\langle k, f \rangle t} \quad (14)$$

for each coordinate of the vector \mathbf{X} , with $k = (k_0, k_1, k_2, k_3) \in \mathbb{Z}^4$, $f = (f_0, f_1, f_2, f_3)$, and $A_{(k)} \in \mathbb{C}$. We can separate these sums in two parts: $x(t) = u(t) + v(t)$ where u does not depend on the resonant frequency f_0 , and v has all the terms depending on f_0 .

$$\begin{cases} u(t) = \sum_{(k), k_0=0} A_{(k)} E^{i\langle k, f \rangle t}, \\ v(t) = \sum_{(k), k_0 \neq 0} A_{(k)} E^{i\langle k, f \rangle t}. \end{cases} \quad (15)$$

The quasi-periodic orbit described by $\mathbf{U}(t)$ is precisely living on a 3-torus which has the characteristics we are looking for. However it is probably not a solution of the equations of motion. But we can assume that it is close to one. Hence, we can use $\mathbf{U}(0)$ as a new initial condition, and obtain a new resonant quasi-periodic orbit $\mathbf{X}'(t)$ with:

$$\mathbf{X}'(0) = \mathbf{U}(0). \quad (16)$$

The amplitude of the resonant terms in this new orbit will be smaller. In other words, it lives on 4-torus closer to the 3-torus of the center of libration. We can then iterate this procedure to suppress all the terms with f_0 .

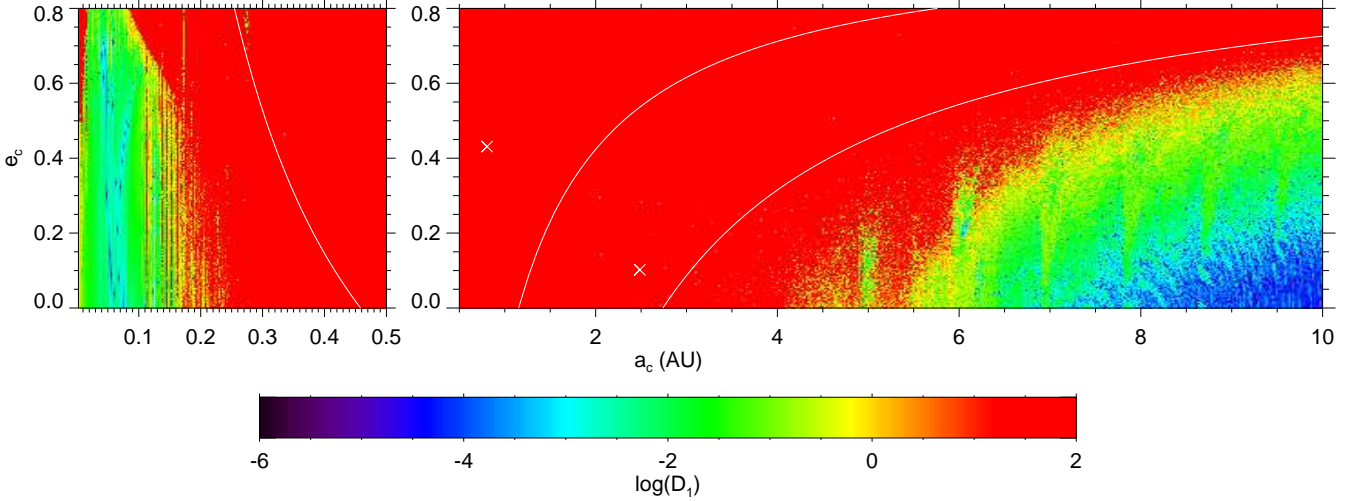


Fig. 8. Mean motion diffusion of tests particles. integration S2 solution with massless particles over 16000yr. We compute two determination n and n' of each particules mean motion over two consecutive time intervals of 8000 yr. The color scale code the stability index $\log |n - n'|$. Initial conditions for the massless particles are $(i_p, M_p, \omega_p, \Omega_p) = (90^\circ, 0^\circ, 0^\circ, 0^\circ)$. On both panel we vary the initial eccentricity of the test particules from 0 to 0.8 with a step size of 0.004. On the left panel the semi-major axis varies from 0.05 AU to 0.5 AU with a step size of 0.0025 AU, and on the right panel it varies from 0.5 AU to 10 AU with a step size of 0.05. The white crosses mark the position of the two planets, and the collision lines are traced with white lines.

4.5.3. Application to HD202206

We present here its application to the HD202206 system, using our orbital solution **S2** as a starting resonant orbit. We work with the $\mathbf{X} = (a_b, \lambda_b, z_b, a_c, \lambda_c, z_c)$ state vector, where $z_b = e_b E^{i\varpi_b}$ and $z_c = e_c E^{i\varpi_c}$. Each step p of the method is decomposed as follows:

- Numerical integration of $\mathbf{X}^{(p)}$,
- Determination of (f_0, f_1, f_2, f_3) using frequency analysis,
- Quasi-periodic decomposition: $x^{(p)}(t) \approx u^{(p)}(t) + v^{(p)}(t)$,
- New initial conditions: $x^{(p+1)}(0) = x^{(p)}(0) - v^{(p)}(0)$

The initial conditions are not computed exactly following Eq. 16. Since we work with a finite number of terms, and the amplitudes of the terms in $v(t)$ are supposed to become small, the error we make because we only take into account that a finite number of terms will be smaller.

The convergence proved to be fast as we reduced the amplitude of the most important resonant terms by 2 orders of magnitude in just 4 steps (Fig. 11). We show graphically the decreasing amplitude of libration at each step in Fig. 10 where we plot approximated sections of the successive torus projected in the (a_c, ϖ_c) plane. No resonant terms are found in the first 100 terms of the quasi-periodic decomposition of each variable at the last step (with the exception of λ_b). In fact, in half of the variables, there are no resonant terms left in the first 300 terms (Fig. 11).

Once we find an orbit with a zero amplitude libration mode to a good approximation, we also get the 3-Torus it is living on since its quasi-periodic decomposition gives us a parametrization of the torus. The three angular variables of the torus appears in the decomposition:

$$\begin{cases} \phi_1 = f_1 t + \psi_1 \\ \phi_2 = f_2 t + \psi_2 \\ \phi_3 = f_3 t + \psi_3 \end{cases} \quad (17)$$

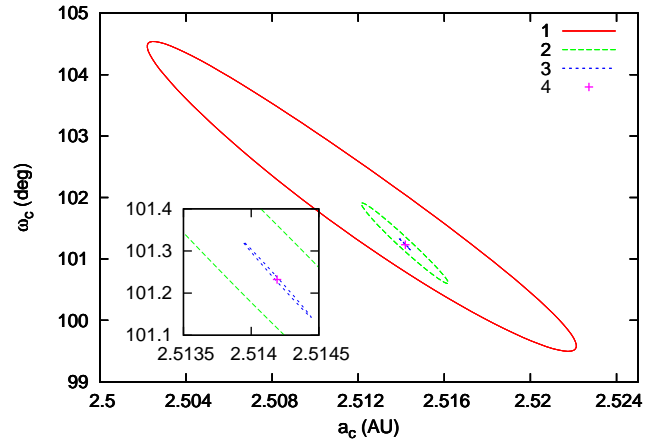


Fig. 10. Projection of a section of the 4-torus of each step's trajectory in the (a_c, ω_c) plane. Each torus is approximated using a (truncated) quasi-periodic decomposition of the trajectory.

where ψ_1, ψ_2 , and ψ_3 are initial phases. Let $\xi_k = E^{i\phi_k}$. We can rewrite Eq. 14 to reveal the underlying torus:

$$x(\phi_1, \phi_2, \phi_3) = \sum_{(k)} A_{(k)} \xi_1^{\alpha_{(k)}} \xi_2^{\beta_{(k)}} \xi_3^{\gamma_{(k)}} \quad (18)$$

Of all the orbits living on this torus we can choose the closest to the radial velocity data. This can be done by minimizing the χ^2 on the three initial phases ψ_1, ψ_2 , and ψ_3 .

We note **S3** the orbit obtained that way at step 6. We give initial conditions for **S3** in table 5. This solution yields a square root of reduced χ^2 equal to 1.55. If the system is locked in the 5:1 mean motion resonance, the libration mode is likely to be dampened through dissipative processes. In that regard, the solution **S2** is unlikely as it is on the edge of the resonant island, and exhibit high resonant mode amplitude (40° for the resonant critical angle). We expect that the real solution will be closer to **S3**.

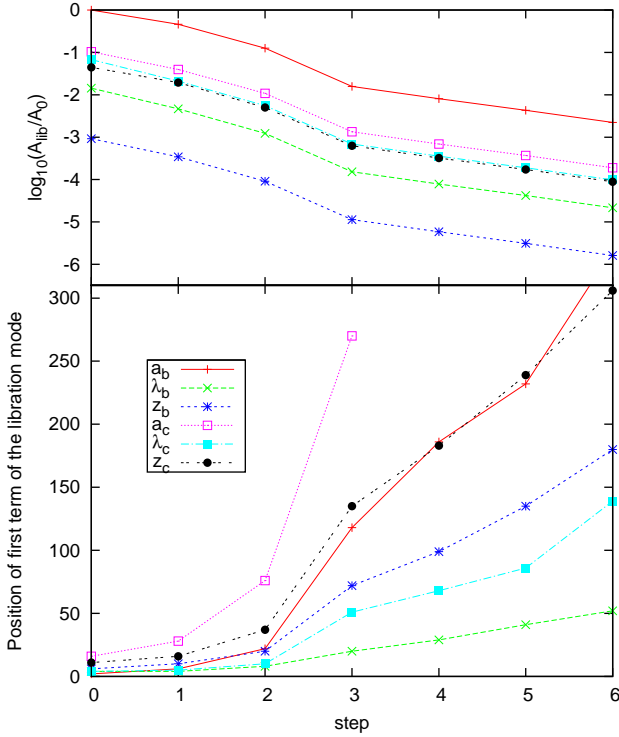


Fig. 11. Evolution of the amplitude of the libration mode in the quasi-periodic decomposition of each variable at each step. In the top panel we plot the relative amplitude of the first term depending on f_0 compared to the first not constant term. In the bottom panel we plot the position of this first term in the decomposition. The first step (abscissa 0) is the **S2** orbital solution, and the last step (abscissa 6) is the orbital solution **S3** (table 5).

Table 5. Orbital parameters of an orbit close to the center of libration of the 5:1 mean motion resonance. This orbit was obtained from **S2** (Table 2) at the sixth iteration. We expect that the actual system will be closer to this orbit as dissipative processes will have dampened the resonant mode.

Param.	S3	inner	outer
a	[AU]	0.8050	2.5113
i	[deg]	90	90
e		0.439	0.071
$M + \omega$	[deg]	239.25	247.30
ω	[deg]	161.81	78.19
Ω	[deg]	0	0
m	[M_{Jup}]	16.59	2.179
Date	[JD-2400000]	53000.00	
$\sqrt{\chi_r^2}$		1.553	

5. Coplanar orbits

5.1. Stability and low χ^2 orbits

In this section we investigate the system behavior when both planets remain in the same orbital plane ($I = 0^\circ$) and are prograde, but the inclination to the line of sight is lower than 90° :

- $i_b = i_c = i \leq 90^\circ$;
- $\Omega_c = 0^\circ$.

For each inclination value, we compute a new best fit with a Levenberg-Marquard algorithm. The $\sqrt{\chi_r^2}$ value obtained at dif-

ferent inclinations is plotted in Fig. 13 (solid line). Interestingly enough, we obtain better fits for lower inclination down to 15° .

In this configuration, the masses of the two companions grow approximately in proportion with $1/\sin i$ when the inclination i diminishes. There is thus very little changes between 90° and 50° , as seen in Fig. 12 (two top leftmost panels). For lower inclinations, due to the increased masses, mutual perturbations become stronger, and less orbits are stable. However, amongst the lowest $\sqrt{\chi_r^2}$ orbits, the ones in the 5:1 mean motion resonance remain stable for inclinations up to 15° .

For $i = 10^\circ$, no stable orbits are left (bottom rightmost panel). This puts clear limits on the inclination of the system, and on the masses of the two companions : $m_b < 95.5 M_{\text{Jup}}$ and $m_c < 12.5 M_{\text{Jup}}$.

An interesting property showing in Fig. 12 is that the lowest χ^2 orbits are always in the vicinity of the stable island of the 5:1 mean motion resonance, for all inclinations. We believe that it is a strong point supporting the hypothesis of a HD202206 system locked in this resonance. It appears however, that after $i = 50^\circ$, and for lower inclinations, the low χ^2 region is slightly shifted towards lower a_c values than the resonance island.

In order to have a more precise picture, we span i values from 10° to 90° with a step size of 5° . For each inclination value, we start by computing a new best fit with the Levenberg-Marquard algorithm. $\sqrt{\chi_r^2}$ and the stability indexes D_1 and D_2 are computed in the (a_c, e_c) plane of initial conditions, around the best fit. The size of each grid is 101×161 dots, with step sizes of respectively 0.0025 AU and 0.002. For each of these maps, we compute D_{lim} (see section 3.4), and detect stable regions, and their relative positions to the observations in terms of $\sqrt{\chi_r^2}$.

In order to get a synthetic vision of all this data, we can get an estimation of the lowest stable $\sqrt{\chi_r^2}$ for each inclination (Fig. 13). We plot with respect to i the lowest $\sqrt{\chi_r^2}$ of $D_1^s < D_{\text{lim}}$ orbits (broken curve), along with the best fit value (solid curve).

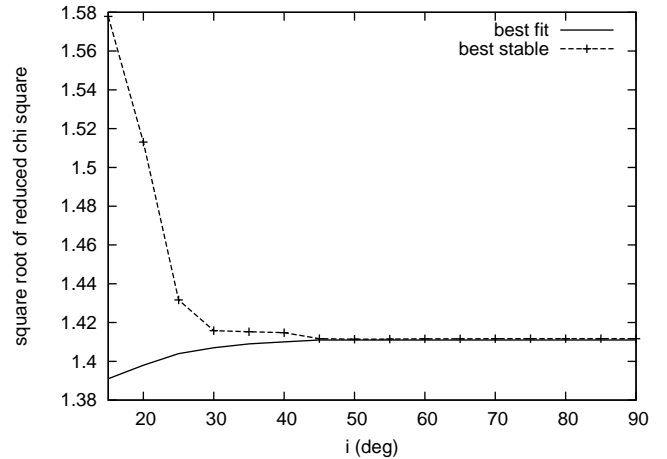


Fig. 13. Evolution of the best fit $\sqrt{\chi_r^2}$ (solid curve) and an estimation of the best stable orbits $\sqrt{\chi_r^2}$ in function of the inclination i . For each value of i between 90° and 10° , a new fit, assuming a coplanar configuration, is computed. We then look for stable orbits around each of these orbital solutions in a (a_c, e_c) plane of initial conditions.

It mainly confirms that the distance between stable orbits, and low $\sqrt{\chi_r^2}$ orbits is really small from 90° to 50° . It is actually slightly better between 60° and 50° .

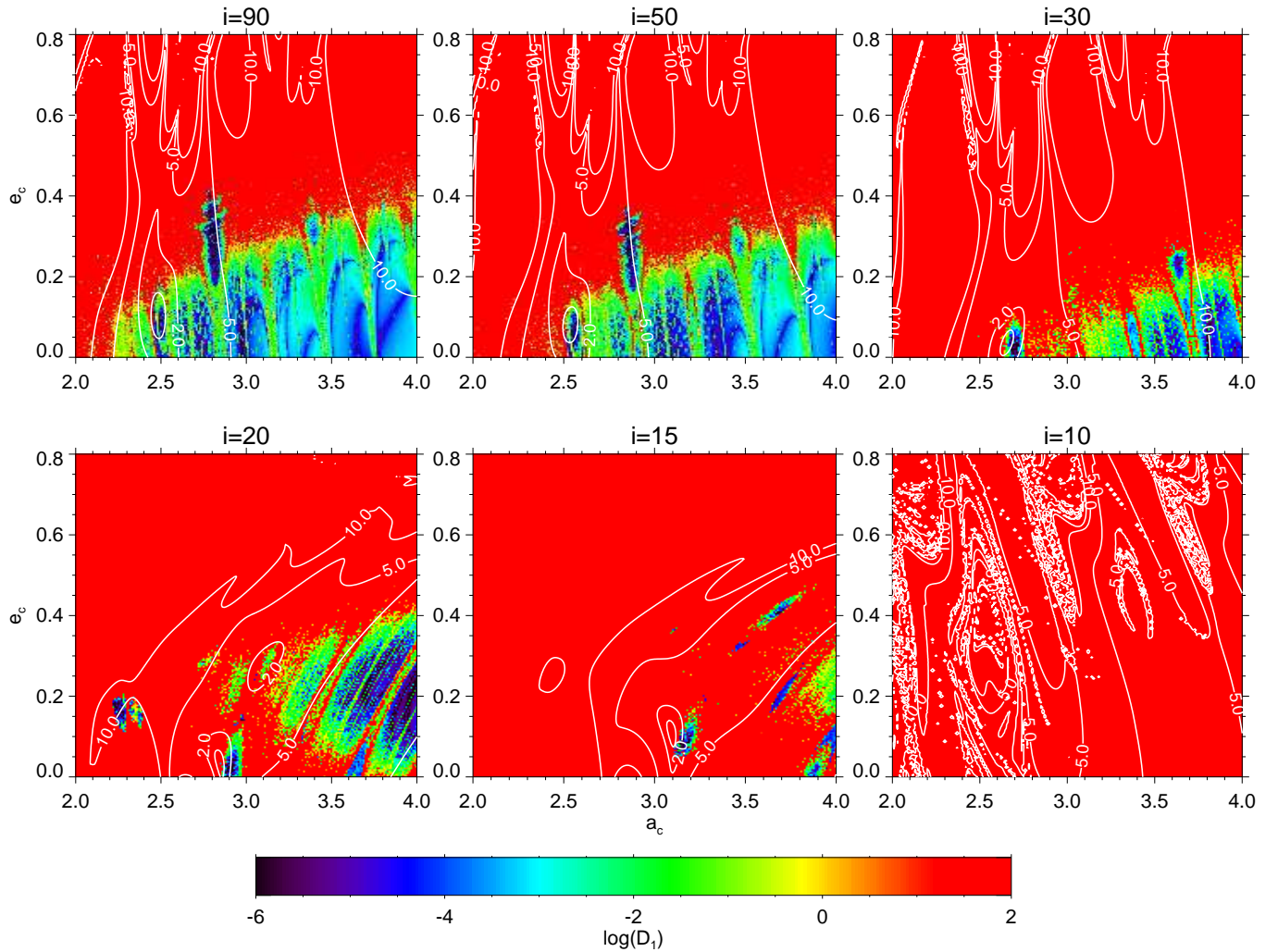


Fig. 12. Dynamics of a coplanar HD202206 system for different value of the inclination i . Each panel is a diffusion map in the (a_c, e_c) plane of initial conditions constructed the same way as the top panel of Fig. 5 (the top-left panel is in fact a copy). For each value of inclination i , a new fit, assuming a coplanar system, is computed.

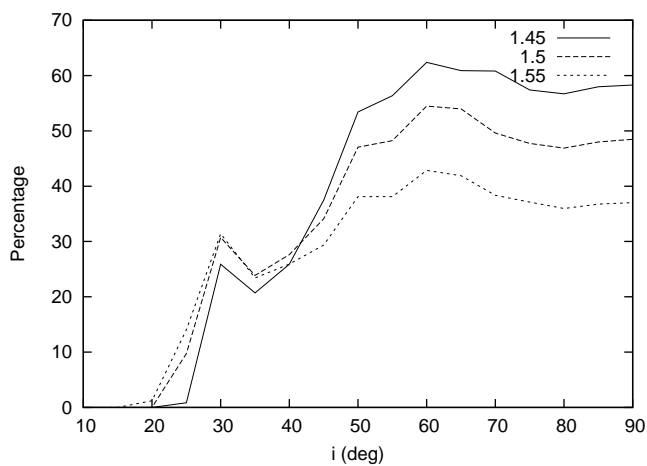


Fig. 14. Percentage of stable orbits inside a given $\sqrt{\chi_r^2}$ level curve against i (see Fig. 13).

To have a better idea of the correlation between low $\sqrt{\chi_r^2}$ orbits and stable orbits, we look at the percentage of stable orbits inside a given $\sqrt{\chi_r^2}$ level curves (Fig. 14). It gives a synthetic rep-

resentation of the overlap between low $\sqrt{\chi_r^2}$ regions and stable regions. It is very clear that inclinations lower than 30° , although possible, are very unlikely. It also appears that inclinations between 90° and 50° are the most probable.

If we limit the acceptable inclinations to $30^\circ \leq i \leq 90^\circ$, we can derive limits for the masses of the inner and outer planets (assuming a coplanar prograde configuration):

$$\begin{aligned} - & 1 \leq m_b/m_b^{(0)} \leq 2 \\ - & 1 \leq m_c/m_c^{(0)} \leq 2 \end{aligned}$$

It is interesting to estimate the time when the radial velocity data will allow to determine a more accurate estimation of the inclination i , and masses for the system. Assuming this model is close enough to the true system, we look at the differences of the radial velocities in the $i = 90^\circ$ case, and $i = 50^\circ$, or $i = 30^\circ$. With the hypothesis of an instrumental precision of 7 m/s, we find (Fig. 15) that we will have to wait until about 2015 to separate between $i = 90^\circ$ and $i = 30^\circ$, which corresponds to approximately a factor 2 in the masses. For $i = 50^\circ$, five more years are needed for the differences between the two configurations to be greater than the measurements precision.

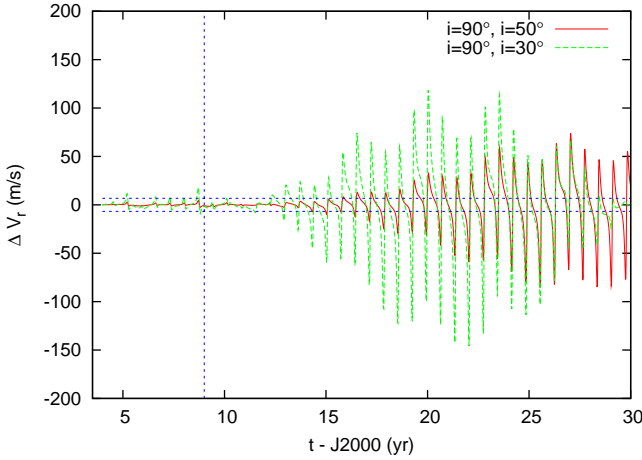


Fig. 15. Differences between the radial velocity of a stable solution with $i = 90^\circ$, and $i = 50^\circ$ (red curve), or $i = 30^\circ$ (green curve). The starting epoch of the three integrations is 2453000.00JD. The blue horizontal lines represents the precision of the current set of data, obtained with the CORALIE instrument. The vertical blue line marks the beginning of 2009.

5.2. Resonant and secular behavior

We end this study of the coplanar configurations with a quick look at the dependence of the resonant and secular dynamics on the inclination. For each inclination, we picked a stable orbit with a low $\sqrt{\chi_r^2}$ value, and plotted its fundamental frequencies l_θ , g_1 , and g_2 in Fig. 16.

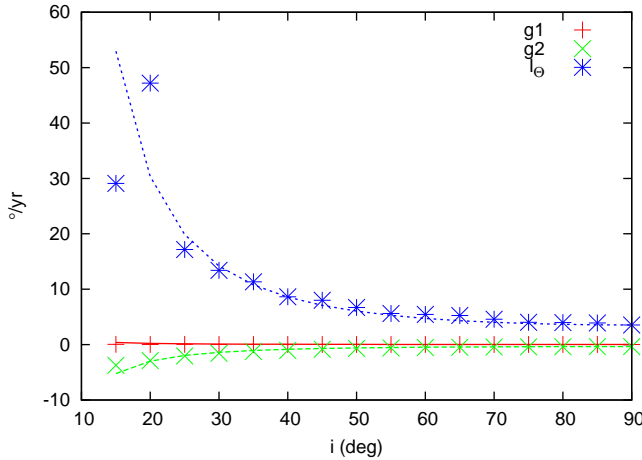


Fig. 16. Libration and secular frequencies. For each inclination i we pick a stable orbit with a low χ^2 and integrate it over 1 million years. Using frequency analysis, we determine for each orbit its fundamental frequencies. The solid curves represent, for each frequency, a $1/\sin^2 i$ law.

As expected from the perturbation theory, when the masses increase, the secular frequencies also increase (in absolute value). We verify that it follows a rule in $1/\sin^2 i$ (solid curve). This is a consequence of the fact that the most important terms responsible for the secular dynamics are of order two of the masses.

6. Mutually inclined orbits

In this section we drop the coplanarity constraint. We allow the inclinations i_b and i_c to vary independently, and we also allow variations of Ω_c , the longitude of ascending node of c . To span the possible values for i_b , i_c , and Ω_c in an efficient manner, we restrict ourselves to two mass ratios k_b (Eq. 3) for planet b :

- $k_b = 1$ ($i_b = 90^\circ$),
- $k_b = 2$ ($i_b = 30^\circ$),

and three mass ratios k_c for planet c :

- $k_c = 1$ ($i_c = 90^\circ$),
- $k_c = 2$ ($i_c = 30^\circ$ or $i_c = 150^\circ$),
- $k_c = 5$ ($i_c = 11^\circ$ or $i_c = 169^\circ$).

For each couple of inclinations i_b and i_c , we let $\Delta\Omega$ vary between 0° and 360° with a 10° step size, and for each triplet $(i_b, i_c, \Delta\Omega)$ we perform a fit with the Levenberg-Marquard minimization, and compute a diffusion grid in the (a_c, e_c) plane of initial conditions around the fit. The step sizes of the grids are respectively 0.0025 AU and 0.004. We plotted in Fig. 17c and Fig. 18c the mutual inclination I as a function of $\Delta\Omega$ for reference. For each configuration we look at the proportion of stable orbits inside the $\sqrt{\chi_r^2} = 1.5$ level curve (Fig 17b and 18b). We will assume that stable zones with $\sqrt{\chi_r^2} \leq 1.5$ orbits harbor potential solutions of the system. Note that we keep the initial inclination i_b in $]0; \pi/2]$ as opposed to i_c (see section 3.1). Also for any given values $\alpha \in]0; \pi/2]$ and $\beta \in [0; 2\pi[$, assuming all the other orbital elements identical, the configuration $(i_b = \pi/2, i_c = \alpha, \Omega_c = \beta)$ is symmetric to the configuration $(i_b = \pi/2, i_c = \pi - \alpha, \Omega_c = -\beta)$ with respect to the plane (\vec{i}, \vec{k}) (see Fig. 2). Since this plane contains the line of sight, the two configurations are indistinguishable using radial velocity measurements. Hence for $k_b = 1$ ($i_b = 90^\circ$) we will not look at $i_c = 150^\circ$ and 169° .

6.1. $k_b = 1$

For $k_b = 1$ ($i_b = 90^\circ$, Fig. 17) we find that significant stable zones inside $\chi^2 = 1.5$ exist mostly for aligned and anti-aligned ascending nodes (i.e. $\Delta\Omega \approx 0^\circ$ and 180° in Fig 17b).

For $k_c = 1$ (red curves) the aligned configurations ($\Delta\Omega = 0^\circ \pm 10^\circ$) are coplanar and prograde ($I \approx 0^\circ$), and the anti-aligned configuration ($\Delta\Omega = 180^\circ \pm 10^\circ$) are coplanar and retrograde. Outside those two particular cases, we find no significant stable zones for $\sqrt{\chi_r^2} \leq 1.5$. Indeed, while the resonant island is roughly centered on the lowest χ^2 level curve, it is not stable outside the coplanar configurations. We find that there exists an extended zone of stability outside the resonance for $\Delta\Omega \approx 30^\circ$, but it lies just outside the 1.5 level curve. Note that due to symmetries, the situation for $\Delta\Omega > 180^\circ$ mirrors that of $\Delta\Omega < 180^\circ$.

For $k_c = 2$ (green curves) we find again stable zones for $\Delta\Omega \approx 0^\circ$, but not around 180° . However stable regions with potential solutions exist for $\Delta\Omega$ values up to 90° , corresponding to mutual inclinations between 60° and 90° . This is mostly due to the minimum χ^2 getting smaller up to $\Delta\Omega = 90^\circ$ (see the green curve in Fig. 17a). While the stable regions, both in the resonance and outside, shrink when $\Delta\Omega$ augments, the $\chi^2 = 1.5$ level curves encompass a larger area.

Finally for $k_c = 5$ (blue curves), no significant stable zones are found at low χ^2 values.

To summarize, potential solutions (stable orbit with a low χ^2) for $i_b = 90^\circ$ mainly exists for coplanar configurations, inside the 5:1 mean motion resonance. If planet c 's mass is kept low

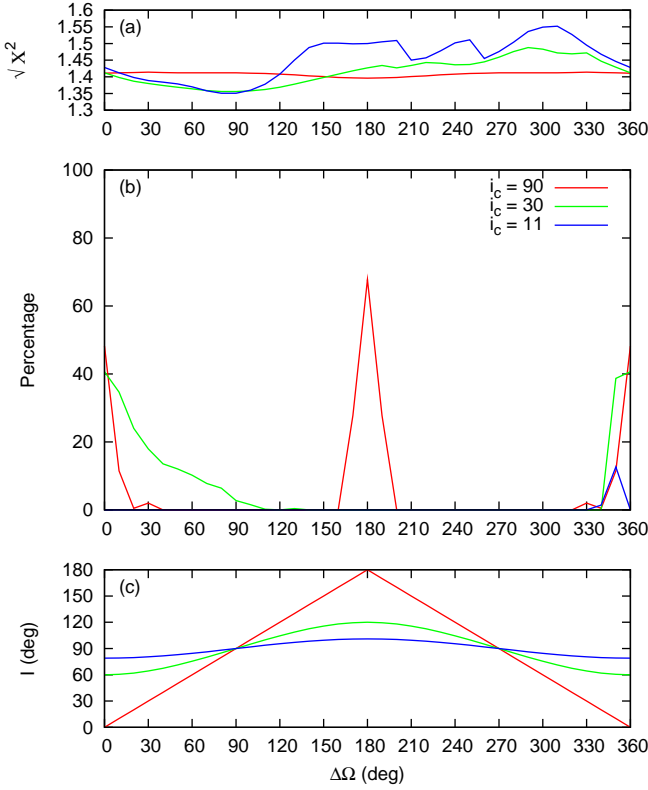


Fig. 17. Stable configurations for $i_b = 90^\circ$, that is for the minimum mass of planet b . For each value of i_c in ($90^\circ, 30^\circ, 11^\circ$), and $\Delta\Omega$ between 0° and 360° we compute diffusion index over grids in the (a_c, e_c) plane of initial conditions with step sizes of respectively 0.0025 AU and 0.004. Each grid is also centered on the minimum χ^2 computed for each couple $(i_c, \Delta\Omega)$. We plot against $\Delta\Omega$ the square root of the minimum χ^2 in the top panel, and the proportion of stable orbits inside $\sqrt{\chi_r^2} = 1.5$ in the middle panel. The mutual inclination corresponding to each triplet $(i_b, i_c, \Delta\Omega)$ is plotted in the bottom panel.

($k_b < 5$) stable regions do exist for non coplanar configurations, but they are located outside the lowest χ^2 region. A noteworthy exception is the retrograde configuration, where stable orbit are only found close to the coplanar case, which only happens for $k_c = 1$ and $\Delta\Omega \approx 180^\circ$.

6.2. $k_b = 2$

When we double the mass of planet b ($i_b = 30^\circ$, Fig.18), once again retrograde potential solutions can only occur for coplanar orbits: $i_c = 150^\circ$, and $\Delta\Omega \approx 180^\circ$ (green dotted curve). Concerning prograde orbits, there exists potential stable solutions for a mutual inclination of $I \approx 60^\circ$:

- $i_c = 90^\circ$ and $\Delta\Omega = 0^\circ$ (red curve),
- $i_c = 30^\circ$ and $\Delta\Omega = 180^\circ$ (green solid curve).

6.3. Conclusions

To sum up we find that the configurations which have a significant stable zone at low χ^2 values are found mostly when the two lines of nodes are aligned. That is for $\Delta\Omega$ close to 0° or 180° . In addition, stable orbits with the lowest χ^2 are all in the 5:1 mean

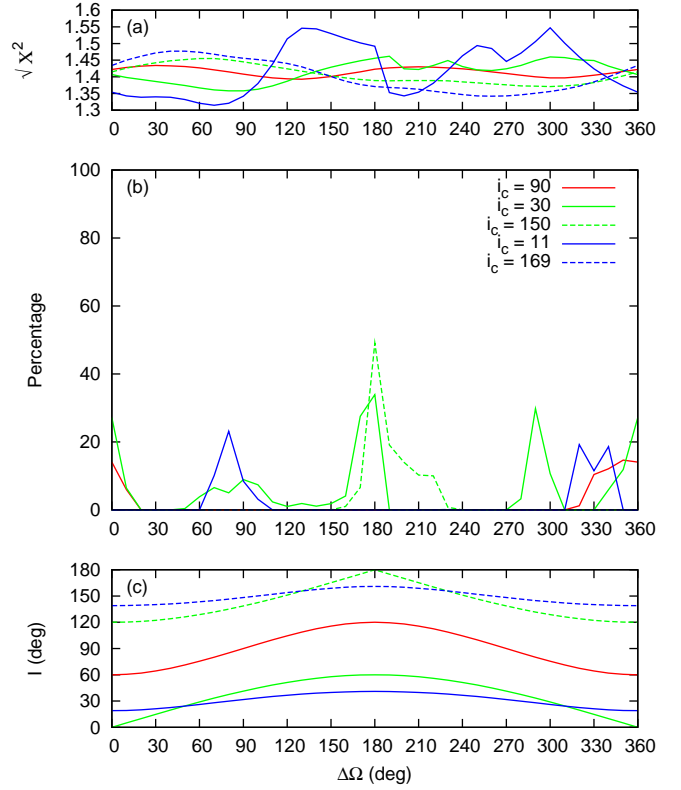


Fig. 18. Stable configurations for $i_b = 30^\circ$, that is for approximately twice the minimum mass: $m_b \approx 33.5 M_{\text{jup}}$. See Fig. 17 caption for more details.

motion resonance except for nearly coplanar retrograde configurations, where they can also be close to the commensurability. However we can also find stable orbits outside the resonance in the prograde resonance, usually with $\sqrt{\chi_r^2}$ higher than 1.45. Retrograde configurations seem to be limited to nearly coplanar orbits with anti-aligned ascending nodes. Other than that, we could not find any clear correlation with mutual inclination.

The fact that we find non-resonant stable solutions for retrograde configurations is consistent with Smith & Lissauer (2009). They have shown that retrograde configurations allow more closely packed systems than prograde configurations. It was also suggested by Gayon & Bois (2008) that retrograde configurations are likely alternatives both from the radial velocity data and the long term stability point of view. Forming such a system remains however difficult, and we will thus not favor this hypothesis.

7. Discussion and conclusion

Assuming that the system is coplanar, we performed a systematic study of the dynamics of the system for different inclinations to the line of sight. We are able to find constraints for the inclination to the line of sight: $30^\circ \leq i \leq 90^\circ$. This means that the companions' masses are most likely not greater than twice their minimum values:

- $1 \leq m_b/m_b^{(0)} \leq 2$
- $1 \leq m_c/m_c^{(0)} \leq 2$

We also studied the influence of mutual inclination for two different inclinations of the planet b ($i_b = 90^\circ$ and $i_b = 30^\circ$), but did

not find any clear correlation other than that retrograde potential stable solution consistent with the radial velocity data seem to be limited to mutual inclinations close to 180° (i.e. nearly coplanar orbits). As Goździewski et al. (2006), we find possible stable solutions with low χ^2 for a wide range of mutual inclinations between 0° and 90° . The current data cannot yield more precise constraints. Also the masses determination is dependent on the stellar mass which is not well established.

Although all published dynamical studies of HD202206 suggest that b and c are in a 5:1 mean motion resonance, it is still a debated question. For instance, Libert & Henrard (2007) assume that it is just close to the commensurability. Libration of $\Delta\varpi$ occurs for particular initial values of this angle, providing a stabilizing mechanism outside the mean-motion resonance, not far from the best fits. In most cases other than retrograde coplanar configurations, those orbits in near-commensurability are worse solutions than the ones in resonance, but they could be more probable if the eccentricities are overestimated (especially for b). We find that all significant stable zones with the best O-C are in the 5:1 mean motion resonance. In fact the minimum χ^2 is almost always in the resonance or very close to it, and stable orbits in the resonance can be found with χ^2 not significantly higher than the best fit. In addition the O-C level curves tend to follow roughly the resonant island, even though the agreement is not as perfect as for the HD45364 system (Correia et al. 2009b). This is an improvement from Correia et al. (2005) where the best fit lay outside the resonant island, and the χ^2 had to be degraded to find a stable solution. We thus believe that the resonant configuration is the most probable. We provide a stable solution (S2, Table 2) in the coplanar edge-on case. This solution shows a high amplitude resonant mode in the libration of the critical angle. We believe that this resonant mode is probably dampened by dissipative processes. We use frequency analysis to find a torus on which such orbits exist. Although the specific orbit we give in Table 5 does not have a very low $\sqrt{\chi_r^2}$ at 1.55, we expect that the true orbit will be close to it with a low libration amplitude.

Note that for retrograde configurations, the picture is quite different. The best fit lies in a very stable region just outside the mean motion resonance. While these orbits are valid candidates from the dynamical and the observational points of view, we do not favor them as the formation of these systems is hard to explain.

We investigated the possibility of undetected companions. We found that planets with masses smaller than approximately one Neptune mass can exist for semi-major axis lower than 0.12 AU. $0.5 M_{Jup}$ planets are also possible beyond 6.5 AU. No planets are possible between 0.12 AU and 6.5 AU as they would be unstable. The two planets model may prove to be wrong in the future, but these hypothetical new companions should not have a big impact on the already detected ones.

Acknowledgements. We acknowledge support from the Swiss National Research Found (FNRS), French PNP-CNRS, and Genci/CINES.

References

- Correia, A. C. M., Couetdic, J., Laskar, J., et al. 2009a, A&A, accepted
 Correia, A. C. M., Udry, S., Mayor, M., et al. 2009b, A&A, 496, 521
 Correia, A. C. M., Udry, S., Mayor, M., et al. 2005, A&A, 440, 751
 Fienga, A., Manche, H., Laskar, J., & Gastineau, M. 2008, A&A, 477, 315
 Gayon, J. & Bois, E. 2008, A&A, 482, 665
 Goździewski, K., Konacki, M., & Maciejewski, A. J. 2006, ApJ, 645, 688
 Goździewski, K. & Maciejewski, A. J. 2001, ApJ, 563, L81
 Henon, M. 1974, Celestial Mechanics, 10, 375
 Henon, M. 1997, Generating Families in the Restricted Three-Body Problem, ed. M. Henon
 Ji, J., Li, G., & Liu, L. 2002, ApJ, 572, 1041
 Laskar, J. 1990, Icarus, 88, 266
 Laskar, J. 1993, Phys. D, 67, 257
 Laskar, J. 1999, in NATO ASI Hamiltonian Systems with Three or more Degrees of Freedom, ed. C. Simo (Kluwer), 134–150
 Laskar, J. 2003, ArXiv Mathematics e-prints
 Laskar, J. & Robutel, P. 2001, Celestial Mechanics and Dynamical Astronomy, 80, 39
 Laughlin, G. & Chambers, J. E. 2001, ApJ, 551, L109
 Lee, M. H. & Peale, S. J. 2002, ApJ, 567, 596
 Lestrade, J.-F. & Bretagnon, P. 1982, A&A, 105, 42
 Libert, A.-S. & Henrard, J. 2007, A&A, 461, 759
 Press, W. H., Teukolsky, S. A., Vetterling, W. T., & Flannery, B. P. 1992, Numerical recipes in FORTRAN. The art of scientific computing (Cambridge: University Press, 2nd ed.)
 Smith, A. W. & Lissauer, J. J. 2009, Icarus, 201, 381
 Sousa, S. G., Santos, N. C., Mayor, M., et al. 2008, A&A, 487, 373
 Udry, S., Mayor, M., Naef, D., et al. 2002, A&A, 390, 267